

Research Article

Fast Backprojection Filtration Algorithm in Circular Cone-Beam Computed Tomography

Xianchao Wang , Yong Zhang, Xingyong Hong, and Honghai Wang

School of Computer and Artificial Intelligence, Chaohu University, Hefei 238024, China

Correspondence should be addressed to Xianchao Wang; xc_wang@aliyun.com

Received 24 March 2023; Revised 6 October 2023; Accepted 17 October 2023; Published 23 October 2023

Academic Editor: Mehtab Singh

Copyright © 2023 Xianchao Wang et al. This is an open access article distributed under the Creative Commons Attribution License, which permits unrestricted use, distribution, and reproduction in any medium, provided the original work is properly cited.

In order to meet the heavy backprojection calculation of the backprojection filtration (BPF) algorithm in circular cone-beam computed tomography (CT), a fast backprojection method is developed, which uses the integral operator of the fixed scanning angle integral interval. The proposed method combines with Hilbert filtration and the filter of the Blackman window, and then, the fast BPF (F-BPF) algorithm is obtained. The experimental results of simulation data and real data demonstrate that the proposed algorithm is fast enough for high-quality reconstructed images only with half-circle projection data.

1. Introduction

Cone-beam computed tomography (CT) technologies have been widely applied in different applications [1–3], such as micro-CT and cone-beam tomography used in radiotherapy [4–6]. It is common that the size of the field of view (FOV) is smaller than that of an imaging object, which leads to transverse truncation in projection data. From such truncated data, conventional reconstruction algorithms will generate various truncation artifacts, such as Feldkamp–Davis–Kress (FDK) algorithm [7]. Even the iterative algorithm also gives inaccurate images [8–10].

In recent years, the backprojection filtration (BPF) algorithm for the reconstruction of CT images was proposed based on PI-line segments in helical cone-beam CT [11–13], which could realize the accurate reconstructed images of the region of interest (ROI) [14, 15]. Due to the wide application of circular cone-beam CT [16, 17], the BPF algorithm is extended to the image reconstruction of circular cone-beam CT on account of virtual PI-line segments [18]. The extended BPF algorithm reconstructs the exact reconstructed images in the middle plane and the approximate reconstructed images in the nonmiddle planes. It provides a way to solve

the image reconstruction of truncation data caused by limited FOV size [19].

In the process of the implementation of the BPF algorithm in circular cone-beam CT, the scanning angles of the two end points of each PI-line segment are different and need to be calculated. The scanning angle integration interval of all reconstructed points in the backprojection calculation of the FDK algorithm is the same. However, the scanning angle integration interval of the points on different PI-line segments in the backprojection calculation of the BPF algorithm is different. It causes the heavy cost of the backprojection calculation and the difficulty of implementation using parallel computation [20]. The problem obstructs the use of the BPF algorithm in practical circular cone-beam CT, although the BPF algorithm can realize the image reconstruction with truncation data in a short scan [21]. To solve it, the fast BPF (F-BPF) algorithm was developed and verified with numerical simulation and the real data reconstruction in this paper.

The rest of the paper is arranged as follows: The theory of the conventional BPF algorithm and the F-BPF algorithm is described in Section 2. Both numerical simulation and real data reconstruction are carried out to demonstrate the proposed algorithm in Section 3. Finally, a conclusion is given in Section 4.

2. Theory

In the following, we briefly introduce the conventional BPF algorithm and then propose the F-BPF algorithm in circular cone-beam CT.

2.1. Conventional BPF Algorithm. The implementation of the conventional BPF algorithm mainly includes two steps. The first step is to calculate the backprojection of the derivatives of the weighted projection data on PI-line segments. The second step is to perform finite Hilbert filtering on the backprojection data along the PI-line segments. The reconstruction formula of the BPF algorithm is given as follows [22]:

$$f(\vec{r}) = \int_{R^3} d\vec{r}' K(\vec{r}, \vec{r}') g(\vec{r}'), \quad (1)$$

$$f(x_c, \lambda_1, \lambda_2) = \frac{1}{2\pi} \frac{1}{\sqrt{(x_{c2} - x_c)(x_c - x_{c1})}} \times \left[\int_{x_{c1}}^{x_{c2}} \frac{dx'_c}{\pi(x_c - x'_c)} \sqrt{(x_{c2} - x'_c)(x'_c - x_{c1})} g(x'_c, \lambda_1, \lambda_2) + 2C \right], \quad (3)$$

where $(x_c, \lambda_1, \lambda_2)$ is another representation of \vec{r} with its coordinates on the PI-line segment, C denotes the projection value along the PI-line segment, and $(x_{c1}, \lambda_1, \lambda_2)$ and $(x_{c2}, \lambda_1, \lambda_2)$ are the representations of two end points of the PI-line segment.

where $f(\vec{r})$ is the image function, \vec{r} is the vector of a reconstruction point, $K(\vec{r}, \vec{r}')$ expresses the integral kernel, and $g(\vec{r}')$ is the backprojection function. Its formula is given as follows:

$$g(\vec{r}) = \int_{\lambda_1}^{\lambda_2} \frac{ds}{|\vec{r}' - \vec{r}_0(s)|} \left. \frac{\partial}{\partial q} \overline{D}(\vec{r}_0(q), \vec{\beta}) \right|_{q=s}, \quad (2)$$

in which $\overline{D}(\vec{r}_0(q), \vec{\beta}) = \int_{-\infty}^{\infty} dt f(\vec{r}_0(q) + t\vec{\beta})$, $\vec{r}_0(s)$ expresses the X-ray source, $\vec{\beta}$ is the unit vector along the direction from $\vec{r}_0(s)$ to \vec{r}' , and λ_1 and λ_2 are the projection angles of the two end points on the PI-line segment.

Combining (1) and (2), the reconstruction formula of the conventional BPF algorithm can be written as follows:

Generally, a group of equally spaced parallel segments on different planes are selected as PI-line segments in circular cone-beam CT, where the backprojection formula is written as follows:

$$g(\vec{r}') = \int_{\lambda_1}^{\lambda_2} d\lambda \frac{S^2}{(R - \vec{r}' \cdot \hat{e}_w(\lambda))^2} \left. \frac{\partial}{\partial u_d} \left(\frac{R}{A} P(u_d, v_d, \lambda) \right) + \frac{P(u_d, v_d, \lambda)}{|\vec{r}' - \vec{r}_0(\lambda)|} \right|_{\lambda_1}^{\lambda_2}, \quad (4)$$

where R is the distance from the X-ray source to the rotation axis, S is the distance from the X-ray source to the detector, (u_d, v_d) is the coordinate of the projection of \vec{r}' on the detector, $A = \sqrt{u_d^2 + v_d^2 + S^2}$, and $P(u_d, v_d, \lambda)$ is the projection value of the coordinate position (u_d, v_d) at the scanning angle λ .

2.2. F-BPF Algorithm. In circular cone-beam CT, the conventional BPF algorithm must calculate the projection angles of the two end points of every PI-line segment, which leads to lower reconstruction efficiency and is not conducive to parallel computing. Thus, a fast approximate

backprojection method is proposed by use of the integral function with a fixed integral interval.

The proposed backprojection function is

$$g(\vec{r}') = \int_0^\pi \frac{ds}{|\vec{r}' - \vec{r}_0(s)|} \left. \frac{\partial}{\partial q} \overline{D}(\vec{r}_0(q), \vec{\beta}) \right|_{q=s}, \quad (5)$$

where the line connecting the X-ray source at the views of 0 and π is supposed to be parallel to the PI-line and in the center of the imaging region, which implies that λ_1 is close to 0 and λ_2 is close to π .

From (2) and (5), the absolute uncertainty of new backprojection is obtained by

$$\begin{aligned}
\left| \Delta g(\vec{r}') \right| &= \left| \int_0^\pi \frac{ds}{|\vec{r}' - \vec{r}_0(s)|} \frac{\partial}{\partial q} \overline{D}(\vec{r}_0(q), \vec{\beta}) \right|_{q=s} - \int_{\lambda_1}^{\lambda_2} \frac{ds}{|\vec{r}' - \vec{r}_0(s)|} \frac{\partial}{\partial q} \overline{D}(\vec{r}_0(q), \vec{\beta}) \right|_{q=s} \\
&= \left| \int_{\lambda_2}^\pi \frac{ds}{|\vec{r}' - \vec{r}_0(s)|} \frac{\partial}{\partial q} \overline{D}(\vec{r}_0(q), \vec{\beta}) \right|_{q=s} + \int_0^{\lambda_1} \frac{ds}{|\vec{r}' - \vec{r}_0(s)|} \frac{\partial}{\partial q} \overline{D}(\vec{r}_0(q), \vec{\beta}) \right|_{q=s}.
\end{aligned} \tag{6}$$

Let R_0 be the radius of the imaging object and $R_r = |\vec{r}'|$. It is obvious that $R_r \leq R_0 < R$. The source trajectory and \vec{r}' can be expressed as $\vec{r}_0(\lambda) = (R \sin \lambda, -R \cos \lambda)$ and $\vec{r}' = (R_r \sin \lambda_r, -R_r \cos \lambda_r)$. Thus,

$$\left| \Delta g(\vec{r}') \right| \leq \frac{1}{R - R_r} \left| \int_0^{\lambda_1} \int_{R-R_0}^{R+R_0} \frac{\partial f(\vec{r}_0(q) + t\hat{\beta})}{\partial q} dt ds + \int_{\lambda_2}^\pi \int_{R-R_0}^{R+R_0} \frac{\partial f(\vec{r}_0(q) + t\hat{\beta})}{\partial q} dt ds \right|_{q=s}. \tag{7}$$

We set $C = \max_{|\vec{r}| \leq R_0} |\nabla f(\vec{r})|$. A straightforward computation shows that

$$\begin{aligned}
\left| \Delta g(\vec{r}') \right| &\leq \frac{C}{R - R_r} \left| \int_0^{\lambda_1} \int_{R-R_0}^{R+R_0} \left| \frac{\partial(\vec{r}_0(s) + t\hat{\beta})}{\partial s} \right| dt ds + \int_{\lambda_2}^\pi \int_{R-R_0}^{R+R_0} \left| \frac{\partial(\vec{r}_0(s) + t\hat{\beta})}{\partial s} \right| dt ds \right| \\
&\leq \frac{C}{R - R_r} \left| \int_0^{\lambda_1} \int_{R-R_0}^{R+R_0} \left(\left| \frac{\partial(\vec{r}_0(s))}{\partial s} \right| + t \left| \frac{\partial \hat{\beta}}{\partial s} \right| \right) dt ds + \int_{\lambda_2}^\pi \int_{R-R_0}^{R+R_0} \left(\left| \frac{\partial(\vec{r}_0(s))}{\partial s} \right| + t \left| \frac{\partial \hat{\beta}}{\partial s} \right| \right) dt ds \right| \\
&\leq \frac{2RR_0C}{R - R_r} \left| \int_0^{\lambda_1} \left(1 + \frac{R|\vec{r}' - \vec{r}_0(s)| + R_r R}{|\vec{r}' - \vec{r}_0(s)|^2} \right) ds + \int_{\lambda_2}^\pi \left(1 + \frac{R|\vec{r}' - \vec{r}_0(s)| + R_r R}{|\vec{r}' - \vec{r}_0(s)|^2} \right) ds \right| \\
&\leq \frac{2RR_0C(R_r^2 + 2R^2)}{(R - R_r)^3} (\lambda_1 + \pi - \lambda_2) \\
&\leq \frac{4RR_0C(R_r^2 + 2R^2)}{(R - R_r)^3} |\lambda_1|.
\end{aligned} \tag{8}$$

Note that $|\Delta g(\vec{r}')| \rightarrow 0$ if $\lambda_1 \rightarrow 0$. Actually λ_1 is close to 0, so the new backprojection method is feasible.

By (4), the backprojection of the F-FBP algorithm can be written as

$$g(\vec{r}') = \int_0^\pi d\lambda \frac{S^2}{(R - \vec{r}' \cdot \hat{e}_w(\lambda))^2} \frac{\partial}{\partial u_d} \left(\frac{R}{A} P(u_d, v_d, \lambda) \right) + \frac{P(u_d, v_d, \lambda)}{|\vec{r}' - \vec{r}_0(\lambda)|} \Big|_0^\pi. \tag{9}$$

It is clear that the proposed algorithm possesses three major advantages. First, it just needs the projection views from 0 to π . Second, it reduces the time of data acquisition and reconstruction greatly. Third, similar to the backprojection calculation of the FDK algorithm, the scanning angle integration interval in the backprojection operation of the BPF algorithm is fixed, so the proposed F-BPF algorithm is suitable for parallel computing.

In the F-BPF algorithm, the Hilbert transform is implemented in the frequency domain, which can avoid the oddity in the time domain and improve reconstruction efficiency. The Hilbert transform of $x(t)$ can be written as

$$\hat{x}(t) = \frac{1}{\pi} \int_{-\infty}^{\infty} \frac{x(\tau)}{t - \tau} d\tau = x(t) * \frac{1}{\pi t}, \quad (10)$$

and then,

$$\text{FFT}(\hat{x}(t)) = \text{FFT}(x(t))(-j \text{sgn}(\omega)). \quad (11)$$

Thus, the Hilbert transform of $x(t)$ is

$$\hat{x}(t) = \text{IFFT}(\text{FFT}(x(t))(-j \text{sgn}(\omega))). \quad (12)$$

To reduce or eliminate spectral energy leakage and barrier effects, different window functions are used to truncate the signal. The three commonly used window functions in CT image reconstruction are the Blackman window, the Hanning window, and the Hamming window. The expression for the Blackman window function is as follows:

$$w(n) = \begin{cases} 0.42 - 0.5 \cos\left(\frac{2\pi n}{N}\right) + 0.08 \cos\left(\frac{4\pi n}{N}\right), & 0 \leq n \leq N, \\ 0, & \text{otherwise.} \end{cases} \quad (13)$$

The expression for the Hanning window function is as follows:

$$w(n) = \begin{cases} 0.5 - 0.5 \cos\left(\frac{2\pi n}{N}\right), & 0 \leq n \leq N, \\ 0, & \text{otherwise.} \end{cases} \quad (14)$$

The expression for the Hamming window function is as follows:

$$w(n) = \begin{cases} 0.54 - 0.46 \cos\left(\frac{2\pi n}{N}\right), & 0 \leq n \leq N, \\ 0, & \text{otherwise.} \end{cases} \quad (15)$$

The time-domain diagrams of the Blackman window, the Hanning window, and the Hamming window are shown in Figure 1. It can be seen that the Blackman window function has the fastest sidelobe decrease and can effectively suppress truncation artifacts. The Blackman window is added as the filter to improve the imaging quality in the process of the Hilbert transform [23].

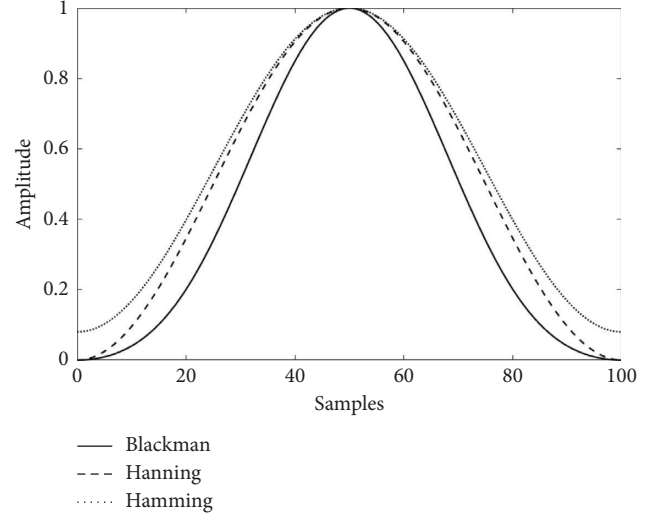


FIGURE 1: Time-domain diagrams of the Blackman window, the Hanning window, and the Hamming window.

3. Experimental Results and Analysis

In order to verify the effectiveness of the proposed F-BPF algorithm, we used simulation data and real data for experiments. The CPU used in the experiments is Intel(R) Core(TM) i5-10210U CPU @ 1.60 GHz.

3.1. Simulation Experiments. In the following, the simulation data were used to verify the effectiveness of the proposed algorithm in this paper. We realized the proposed F-BPF algorithm and the conventional BPF algorithm in MATLAB and analyzed the experimental results of $256 \times 256 \times 256$ standard 3D Shepp–Logan head phantom [24]. The projection data of 360 angles are uniformly generated on the circular scanning trajectory. The conventional BPF algorithm used all the cone-beam projection data, while the F-BPF algorithm used only the data of 180 projection views from 0 to π .

In Figure 2, we display 2D slices in 3D images reconstructed by use of the conventional BPF algorithm and the F-BPF algorithm. Figure 2(a) shows the slice of the 3D Shepp–Logan model, and Figures 2(b) and 2(c) show the slices of the reconstruction results by use of the conventional BPF algorithm and F-BPF algorithm, respectively. In Figure 3, we also show the profiles of the images shown in Figure 2. Figures 3(a) and 3(b) display the profiles of Figure 2(b) on the middle horizontal line and the middle vertical line, respectively. Figures 3(c) and 3(d) show the profiles of Figure 2(c) on the middle horizontal line and the middle vertical line, respectively. The reconstruction and the corresponding real profiles are expressed by the dotted and solid curves, respectively.

The mean square error of the conventional BPF algorithm is 0.0646 and that of the F-BPF algorithm is 0.0694. The time to reconstruct the slice using the conventional BPF

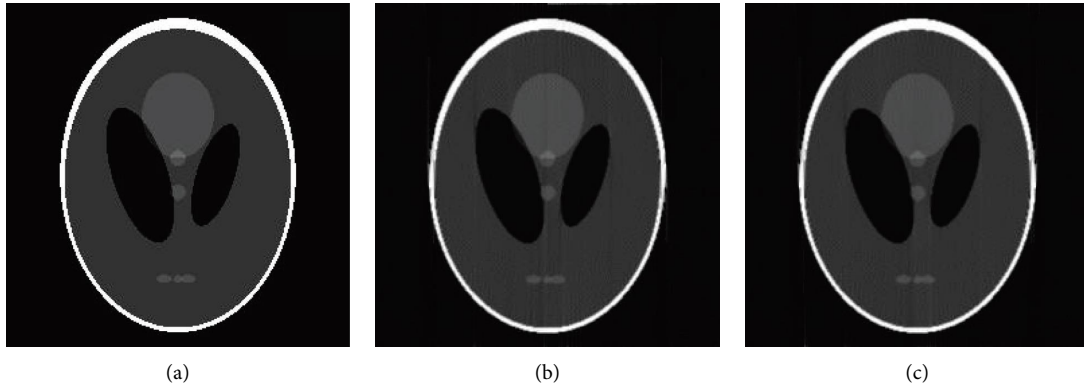


FIGURE 2: Reconstruction images by use of the conventional BPF algorithm and the F-BPF algorithm. (a) Shepp-Logan model. (b) Reconstruction image using the conventional BPF algorithm. (c) Reconstruction image using the F-BPF algorithm.

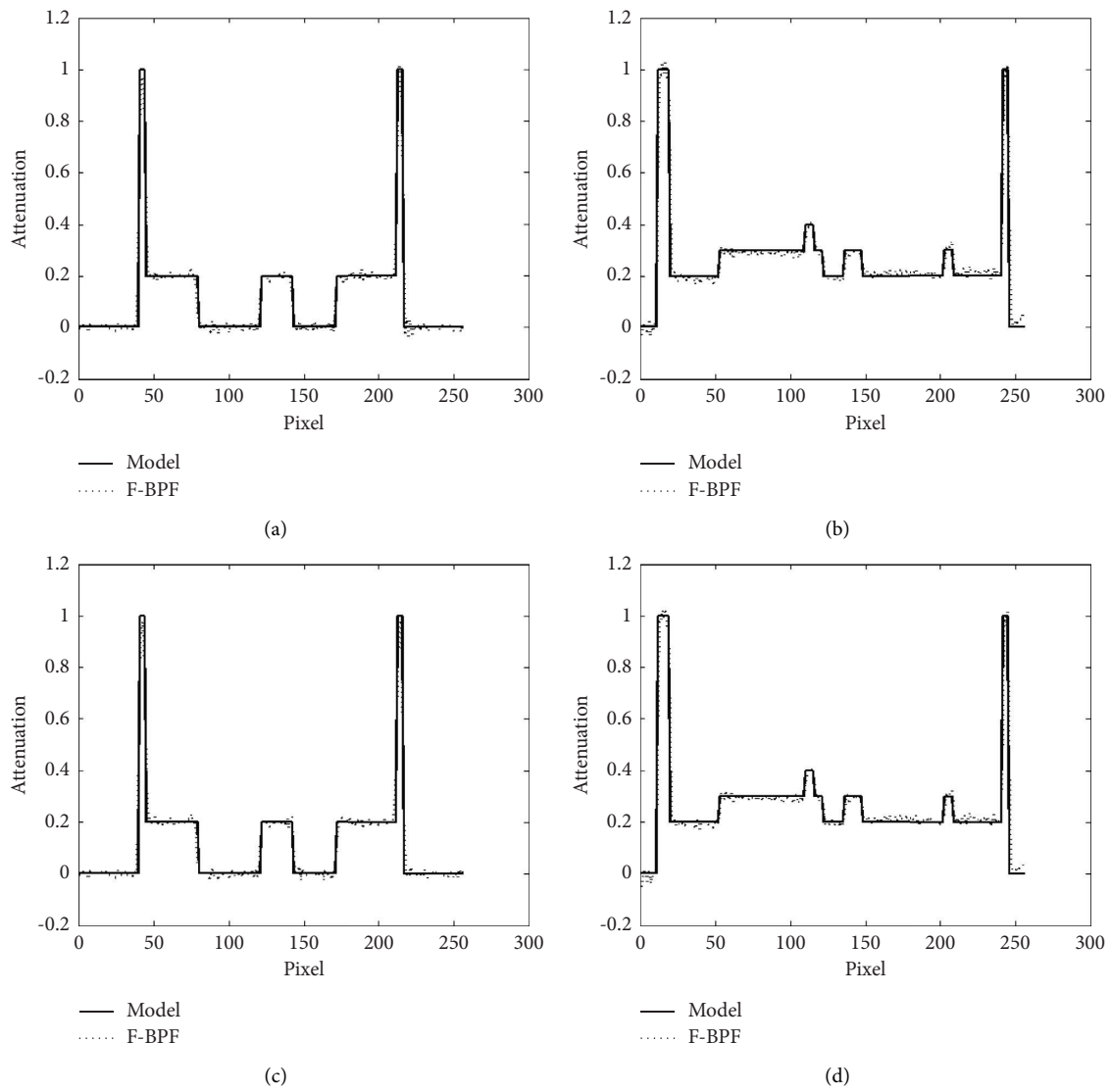


FIGURE 3: Profiles of the reconstruction images in Figure 2. (a) Profile of Figure 2(b) on the middle horizontal line. (b) Profile of Figure 2(b) on the middle vertical line. (c) Profile of Figure 2(c) on the middle horizontal line. (d) Profile of Figure 2(c) on the middle vertical line.

TABLE 1: The experimental results about the parallel performance of the BPF and F-BPF algorithms.

Algorithms	Reconstruction time (CPU) (s)	Reconstruction time (GPU) (s)	Acceleration ratio
BPF	28595.2	98.945	289
F-BPF	1689.6	1.695	997

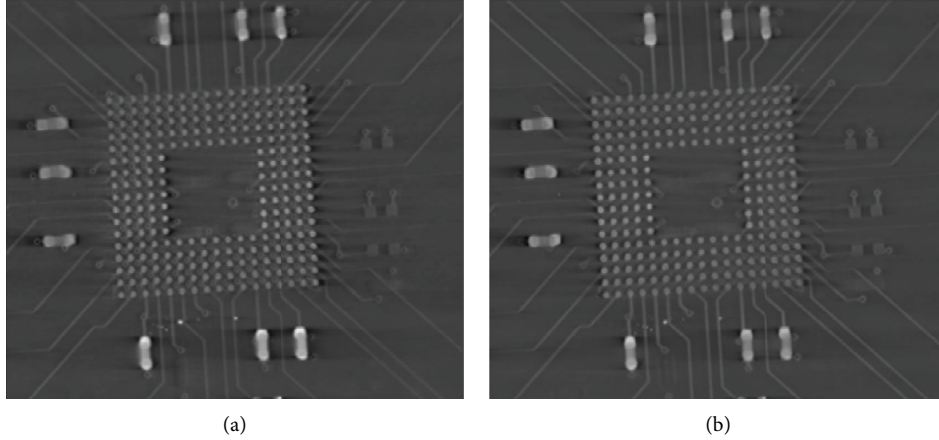


FIGURE 4: Reconstructed images by use of the FDK algorithm and F-BPF algorithm. (a) FDK algorithm. (b) F-BPF algorithm.

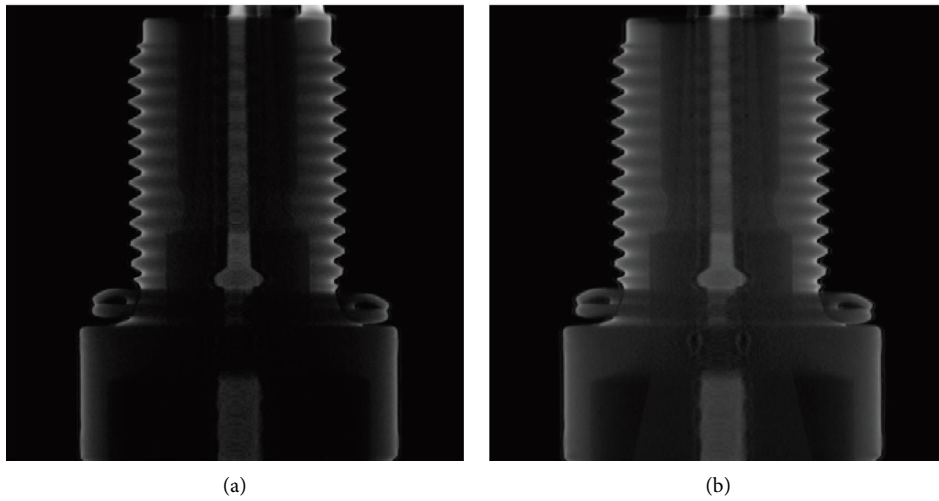


FIGURE 5: Reconstructed images using the F-BPF algorithm. (a) Without the Blackman window. (b) With the Blackman window.

algorithm is 111.7 seconds, while the F-BPF algorithm only costs 6.6 seconds. The simulation experiments prove that the proposed algorithm is effective and that its reconstruction efficiency has been greatly improved in contrast with the conventional BPF algorithm.

The comparative experiments on the parallel performance of the BPF algorithm and the F-BPF algorithm are also conducted, in which the program development software is CUDA 9.0 and the GPU is NVIDIA Tesla K20M. The experimental results are shown in Table 1. It can be seen that the acceleration ratio of the BPF algorithm is 289 and that the acceleration ratio of the F-BPF algorithm is 997. The parallel performance of the F-BPF algorithm is improved compared to that of the BPF algorithm.

3.2. Experiments of Real Data. Next, the real data were used to further verify the effectiveness of the proposed F-BPF algorithm. The real data were obtained using the cone-beam CT system, which used the X-ray source (Hawkeye 130, Thales, France) and the flat-panel detector (4343F, Thales, France) with a pixel size 0.148 mm.

3.2.1. Reconstruction of the Printed Circuit Board. In order to test the performance of F-BPF algorithm, we carried out the experiments to reconstruct the ROI of the printed circuit board (PCB) by the FDK algorithm with the complete data and the F-BPF algorithm with the truncated data. The relevant parameters for experimental data collection were as

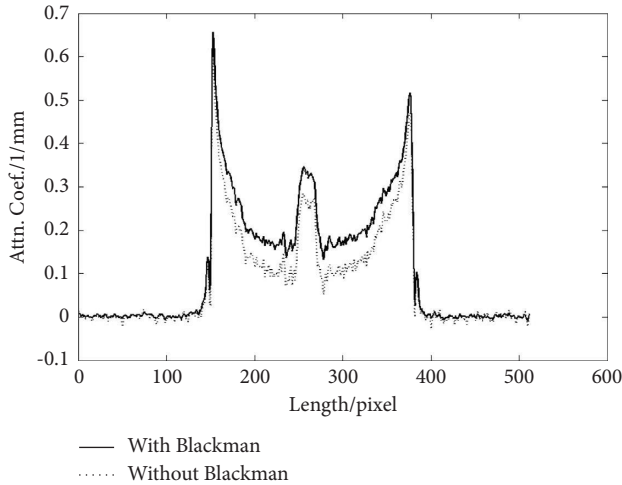


FIGURE 6: Profiles of the reconstructed images in Figure 5 along the middle horizontal line. The solid and dotted curves represent the results obtained with and without the Blackman window, respectively.

follows: The trajectory radius was 477 mm, the distance from the X-ray source to the flat-panel detector was 1265 mm, the size of the ROI was $542 \times 474 \times 284$ voxels, and the projection data of 360 angles were uniformly generated on the circular scanning trajectory. The F-BPF algorithm used 180 projection views from 0 to π , and the FDK algorithm used 180 projection views evenly distributed over the 2π circular trajectory.

Figures 4(a) and 4(b) display 2D slices in 3D images reconstructed by use of the FDK algorithm with non-truncated data and the proposed F-BPF algorithm with truncated data. The reconstruction time of the FDK algorithm is 62 minutes, and the proposed algorithm only costs 41 minutes. From the reconstruction results, the two algorithms reconstruct images with little difference, and the correctness of the proposed algorithm is also demonstrated by real data.

3.2.2. Reconstruction of the Spark Plug. We performed the experiments on a spark plug to compare the reconstruction results with and without the Blackman window in the process of Hilbert filtration. In the circular cone-beam configuration, the trajectory has a radius of 477 mm and a source-detector distance of 1265 mm. The size of the reconstructed ROI is $512 \times 512 \times 512$ voxels. The cone-beam data were generated with 180 projection views uniformly distributed over the π circular trajectory.

In Figure 5, we display the 2D slices in 3D images reconstructed with and without the Blackman window. In Figure 6, we also show the profiles in the images reconstructed by the F-BPF algorithm along the middle horizontal line with and without the Blackman window. Reconstruction quality gets improved after adding the Blackman window. So adding the Blackman window as a filter in Hilbert filtration is effective in reducing noise in real data reconstruction.

4. Discussion and Conclusion

In this paper, we have developed the F-BPF algorithm for image reconstruction in circular cone-beam CT and then performed simulation experiments and real data experiments to validate the proposed algorithm. The results of simulation show that the proposed algorithm is reliable and that its reconstruction efficiency has been greatly improved in contrast with the conventional BPF algorithm. The verification is also demonstrated with real data of PCB, and the images reconstructed by the FDK algorithm and the proposed algorithm are comparable. Considering the noise inevitably exists in real data, the reconstruction results of a spark plug with and without the Blackman window imply that adding the Blackman window is effective in reducing the noise in Hilbert filtration.

The experimental results show that the reconstruction efficiency of the proposed algorithm is a great improvement over the conventional BPF algorithm, and a remarkable merit of the proposed algorithm is that it can be perfectly carried out with only half-circle projection data. Therefore, if the proposed algorithm is used in an industrial cone-beam CT system, it will shorten data acquisition and reconstruction time. If the algorithm is used in medical devices, it will perform well in both saving data acquisition and reconstruction time and reducing their radiation dose to patients.

Data Availability

All the data used to support the findings of the study are included within the article.

Conflicts of Interest

The authors declare that they have no conflicts of interest.

Acknowledgments

This work was supported by the Scientific Research Startup Fund of Chaohu University (No. KYQD-202013), the Natural Science Research Program of Higher Education Institutions of Anhui Province (KJ2021A1029 and KJ2021A1030), the Key Project of the Support Plan for Outstanding Young Talents in Anhui Universities (No. gxyqZD2021130), and the Quality Improvement Project of Chaohu University on Discipline Construction (No. kj21gcx03).

References

- [1] H. Iramina, M. Nakamura, and T. Mizowaki, "Actual delivered dose calculation on intra-irradiation cone-beam computed tomography images: a phantom study," *Physics in Medicine and Biology*, vol. 66, no. 1, Article ID 015007, 2021.
- [2] Y. Park, T. Alexeev, B. Miller, M. Miften, and C. Altunbas, "Evaluation of scatter rejection and correction performance of 2D antiscatter grids in cone beam computed tomography," *Medical Physics*, vol. 48, no. 4, pp. 1846–1858, 2021.

- [3] M. S. Kim, H. P. Hong, Y. R. Lee, J. Y. Choi, K. J. Joo, and Y. S. Cho, "Performance of cone-beam computed tomography (CBCT) renal arteriography for renal tumor embolization," *European Journal of Radiology*, vol. 157, Article ID 110598, 2022.
- [4] X. Zou and B. Wang, "Accurate internal deformation measurement of an indentation test using micro-CT and self-adaptive digital volume correlation," *Applied Optics*, vol. 61, no. 6, pp. 89–98, 2022.
- [5] M. Rossi, G. Belotti, C. Paganelli et al., "Image-based shading correction for narrow-FOV truncated pelvic CBCT with deep convolutional neural networks and transfer learning," *Medical Physics*, vol. 48, no. 11, pp. 7112–7126, 2021.
- [6] C. Altunbas, Y. Park, Z. Yu, and A. Gopal, "A unified scatter rejection and correction method for cone beam computed tomography," *Medical Physics*, vol. 48, no. 3, pp. 1211–1225, 2021.
- [7] L. A. Feldkamp, L. C. Davis, and J. W. Kress, "Practical cone-beam algorithm," *Journal of the Optical Society of America*, vol. 1, no. 6, pp. 612–619, 1984.
- [8] A. L. Cai, Y. Z. Wang, X. Y. Zhong et al., "Total variation combining nonlocal means filtration for image reconstruction in X-ray computed tomography," *Journal of X-Ray Science and Technology*, vol. 30, no. 3, pp. 613–630, 2022.
- [9] Z. Y. Shu and A. Entezari, "Exact gram filtering and efficient backprojection for iterative CT reconstruction," *Medical Physics*, vol. 49, no. 5, pp. 3080–3092, 2022.
- [10] X. C. Wang and C. S. Jiang, "New calculation method for exact length weighting factor in cone-beam computed tomography," *International Journal of Imaging Systems and Technology*, vol. 31, no. 4, pp. 2136–2143, 2021.
- [11] Y. Zou and X. C. Pan, "Exact image reconstruction on PI-lines from minimum data in helical cone-beam CT," *Physics in Medicine and Biology*, vol. 49, no. 6, pp. 941–959, 2004.
- [12] Y. Zou and X. C. Pan, "An extended data function and its generalized backprojection for image reconstruction in helical cone-beam CT," *Physics in Medicine and Biology*, vol. 49, no. 22, pp. 383–387, 2004.
- [13] W. W. Wu, H. Y. Yu, W. X. Cong, and F. L. Liu, "Theoretically exact backprojection filtration algorithm for multi-segment linear trajectory," *Physics in Medicine and Biology*, vol. 63, no. 1, Article ID 015037, 2018.
- [14] X. C. Wang, Z. Y. Tang, B. Yan, L. Li, and S. L. Bao, "Interior reconstruction method based on rotation-translation scanning model," *Journal of X-Ray Science and Technology*, vol. 22, no. 1, pp. 37–45, 2014.
- [15] W. W. Wu, H. Yu, S. Y. Wang, and F. L. Liu, "BPF-type region-of-interest reconstruction for parallel translational computed tomography," *Journal of X-Ray Science and Technology*, vol. 25, no. 3, pp. 487–504, 2017.
- [16] L. Y. Chen, X. Liang, C. Y. Shen, D. Nguyen, S. Jiang, and J. Wang, "Synthetic CT generation from CBCT images via unsupervised deep learning," *Physics in Medicine and Biology*, vol. 66, no. 11, Article ID 115019, 2021.
- [17] I. Romero and C. Q. Li, "A feasibility study of time of flight cone beam computed tomography imaging," *Journal of X-Ray Science and Technology*, vol. 29, no. 5, pp. 867–880, 2021.
- [18] L. F. Yu, Y. Zou, E. Y. Sidky, C. A. Pelizzari, P. Munro, and X. C. Pan, "Region of interest reconstruction from truncated data in circular cone-beam CT," *IEEE Transactions on Medical Imaging*, vol. 25, no. 7, pp. 869–881, 2006.
- [19] H. Kim, J. Lee, J. Soh, J. Min, Y. Wook Choi, and S. Cho, "Backprojection filtration image reconstruction approach for reducing high-density object artifacts in digital breast tomosynthesis," *IEEE Transactions on Medical Imaging*, vol. 38, no. 5, pp. 1161–1171, 2019.
- [20] X. C. Wang, G. E. Hu, B. Yan, Y. Han, L. Li, and S. L. Bao, "Fast low-dose reconstruction from truncated data in dental CT," *IEEE Transactions on Nuclear Science*, vol. 60, no. 1, pp. 174–181, 2013.
- [21] X. C. Wang, H. K. Liu, B. Yan, L. Li, and G. E. Hu, "3D image reconstruction algorithm for truncated projection data in a half-covered scanning configuration," *Insight*, vol. 55, no. 5, pp. 243–248, 2013.
- [22] J. Min, R. Pua, C. Kim et al., "A weighted rebinned backprojection-filtration algorithm from partially beam-blocked data for a single-scan cone-beam CT with hybrid type scatter correction," *Medical Physics*, vol. 46, no. 3, pp. 1182–1197, 2019.
- [23] R. K. Soni, A. Jain, and R. Saxena, "An improved and simplified design of pseudo-transmultiplexer using Blackman window family," *Digital Signal Processing*, vol. 20, no. 3, pp. 743–749, 2010.
- [24] L. A. Shepp and B. F. Logan, "The Fourier reconstruction of a head section," *IEEE Transactions on Nuclear Science*, vol. 21, no. 3, pp. 21–43, 1974.